Extreme Mechanics Letters 44 (2021) 101218

Contents lists available at ScienceDirect

Extreme Mechanics Letters

journal homepage: www.elsevier.com/locate/eml

Ultralow-frequency tunable acoustic metamaterials through tuning gauge pressure and gas temperature

Shaowu Ning [a], Ziming Yan [a], Dongyang Chu [a], Heng Jiang [b,c,*], Zhanli Liu [a,*], Zhuo Zhuang [a]

[a] Applied Mechanics Laboratory, School of Aerospace Engineering, Tsinghua University, Beijing 100084, People's Republic of China
[b] Key Laboratory of Microgravity, Institute of Mechanics, Chinese Academy of Sciences, Beijing 100190, People's Republic of China
[c] University of Chinese Academy of Sciences, Beijing, 100049, People's Republic of China

ARTICLE INFO

Article history:
Received 6 November 2020
Received in revised form 2 February 2021
Accepted 3 February 2021
Available online 11 February 2021

Keywords:
Tunable acoustic metamaterials
Gauge pressure
Gas temperature
Anti-symmetric and symmetric Lamb mode

ABSTRACT

Acoustic metamaterials possessing subwavelength characteristics can be used for low-frequency noise and vibration control. Acoustic metamaterials with adjustable dynamic properties can further enhance their possible applications. This paper designs a kind of tunable acoustic metamaterials consisting of the frame structure, airbag, and balancing weight. And their dynamic characteristics can be manipulated by tuning gauge pressure and gas temperature in the airbag. The calculation results indicate that the tunable acoustic metamaterials can effectively suppress the wave propagation and vibration in the ultralow-frequency band gap (about 13Hz∼90Hz) during manipulation. The complete band gap is the overlapping frequency range of an out-of- and in-plane band gaps. Numerical analyses indicate that the formation of out-of-plane band gap is due to the coupling between the out-of-plane resonant mode of balancing weight and the anti-symmetric Lamb mode of the frame structure. In contrast, the formation of an in-plane band gap is due to the coupling between the in-plane resonant mode of balancing weight and the symmetric Lamb mode of the frame structure. Meanwhile, the manipulation mechanism of these band gaps stems from the fact that through tuning gauge pressure or gas temperature, the structural stiffness of the airbag (torsional stiffness, in-plane, and out-of-plane stiffness) and frame structure (in-plane and bending stiffness) can be significantly tuned so that the modes related to them can be manipulated. The tunable acoustic metamaterials can be used for active control of low-frequency vibration and noise. It is possible to provide guidelines for designing other acoustic metamaterials to suppress low-frequency vibration and noise.

© 2021 Published by Elsevier Ltd.

1. Introduction

Phononic crystals (PnCs) and acoustic metamaterials (AMMs), which are artificially engineered structures that exhibit physical properties not available in natural materials, possess the excellent manipulation performance to elastic wave propagation in these structures. Rationally designed PnCs and AMMs can realize some interesting phenomena, such as negative refraction [1–3], self-collimation of wave [4], low-frequency super absorption [5,6], negative equivalent material parameters [6–12], and so on. They can potentially serve for enabling various applications, such as waveguide [13,14], super-resolution imaging [15,16], cloaking [17,18], wavefront modulation [19], noise and vibration control [20,21] and so on. From the view of the formation mechanisms of band gaps, the PnCs usually possess the Bragg scattering band gaps caused by periodic variation in the impedance of the elastic medium, and they can attenuate waves with a wavelength of the same dimensions as their periodic unit cell sizes [22]. For AMMs, not necessarily periodic, they are material systems with internal resonating elements. The greater importance is that they can attenuate waves much larger than their unit cell sizes [6]. The dynamic performance of AMM possessing the subwavelength characteristic can be described by both dynamically equivalent material parameters and band structure. The rationally designed AMMs can realize negative effective density [6,11,23], negative effective modulus [10,24], double negative [7–9] and even zero equivalent material parameters [12]. The PnCs and AMMs possess the band gap characteristics, in which waves cannot propagate, so that they have potential applications in noise and vibration control [20,21,25], seismic protection [26–28], and so on. Especially, the resonant AMM is more suitable for controlling the low-frequency (<500 Hz) noise and vibration because of its subwavelength characteristic.

However, many studies mainly focus on passive PnCs and AMMs with constant properties. Their dynamic properties are difficult to change once they are fabricated, resulting in a fixed

* Corresponding authors.
E-mail addresses: hengjiang@imech.ac.cn (H. Jiang), liuzhanli@tsinghua.edu.cn (Z.L. Liu).

https://doi.org/10.1016/j.eml.2021.101218
2352-4316/© 2021 Published by Elsevier Ltd.

and narrow working band gap and limiting their applications. Thus, there has been interested in developing tunable PnCs and AMMs with properties tuned on demand. The typical design schemes of tunable PnCs and AMMs include reconfigurable design scheme and multi-physical field coupling design scheme. Based on multi-physical field coupling design scheme, including magnetic and/or electric field [29–33], temperature [24], piezo shunting [14,20,34], pre-stress field [35–37], and so on, many kinds of tunable PnCs and AMMs have been designed. The typical realization approaches of the reconfigurable PnCs and AMMs include rearrangement of unit cell [38–40], structural instability [41–48], multistable system [49–52], and so on. For example, Wu et al. [40] studied the effects of the rotation of weak symmetry scatterers in the gas or fluid medium on band structures of PnCs. Meanwhile, it has been studied extensively that mechanical instabilities may induce geometry reconfiguration (pattern transformations) of the architectures. They can be exploited to alter the propagation of elastic waves or the direction of wave propagation, as in Ref. [42,43,45,46]. However, the deformed reconfigurations of the architectures require an external stimulus to sustain their deformations. Thus, to design the architectures with the shape memory effect, an alternative approach is to develop a multistable material consisting of multiple bistable elements, which can maintain a deformed configuration after removing the external stimulus. Based on a multistable system, Meaud and Che [51] have designed the reconfigurable architected materials formed by a one-dimensional chain of bistable unit cells. These architected materials have multiple stable configurations so that they have unique dispersion relations in the undeformed and fully deformed stable configurations. However, for the above reconfigurable PnCs and AMMs, they need the large deformation of structures to implement the tunable dynamic performance. In practical application, the implementation of large deformation is also tricky, and even the large deformation of construction is not acceptable. At present, there is work to improve this situation. Huang et al. [53] have designed a soft PnC plate with spring-mass-like resonators, in which substantial modification of band gaps under small deformation can be achieved through deliberate structural design. Differently, in this paper, the AMM consisting of the frame structure, airbag, and balancing weight is also designed to overcome the shortcoming, as shown in Fig. 1. Airbags are widely used for tires, air-spring, soft robots, and so on. Utilizing a ring-shaped airbag as a connecting structure between frame structure and balancing weight, we can manipulate the dynamic response of AMM through tuning gauge pressure in the airbag without the large deformation of the matrix (frame structure). Besides, the temperature is another critical parameter for the gas medium, and it can also be used to tune the dynamic performance of AMM. Namely, the dynamic performance of the tunable AMM presented in this paper can be adjusted simultaneously by tuning gauge pressure and gas temperature.

Low-frequency (<500 Hz) vibration and noise attenuation is a goal of environmental and architectural engineering. However, in this frequency range, to achieve the ideal noise and vibration attenuation, it requires high mass and thickness structures, which is not acceptable. We have known that the rationally designed locally resonant AMM possessing the sub-wavelength band gap characteristic can achieve low-frequency vibration and noise attenuation. For the AMM presented in this paper, we focus on its low-frequency band gap characteristic and investigate its manipulation performance through tuning gauge pressure and gas temperature. We have found that the AMM possesses the ultra low-frequency locally resonant band gaps (about 13 Hz∼90 Hz), and it can be effectively manipulated through tuning gauge pressure and gas temperature. Thus, it can be used for the suppression of low-frequency vibration and noise. Through the research, it is possible to provide useful guidelines for designing other forms of AMMs to suppress low-frequency noise and vibration. Next, we will give the design scheme and analytical process in detail.

Table 1
The Ogden parameters of the neoprene airbag.

i	α_i	μ_i (MPa)	D_i
1	1.3	0.4095	0.2367
2	5.0	0.003	0
3	−2.0	0.01	0

2. Design scheme of tunable acoustic metamaterial

Fig. 1 shows the designed AMM consisting of three components: frame structure, airbag and balancing weight. The three components are connected by tie constraint (ABAQUS/Interaction, *Tie) [54]. The frame structure is made of aluminum and its density, Young's modulus and Poisson's ratio are 2700 kg/m^3, 71 GPa and 0.33, respectively. The balancing weight is made of tungsten and its density, Young's modulus and Poisson's ratio are 19100 kg/m^3, 354.1 GPa and 0.35, respectively. The airbag is made of neoprene and its density is 1240 kg/m^3. The response of the neoprene is captured by an Ogden model [55]. The form of the Ogden strain energy potential is

$$U = \sum_{i=1}^{N} \frac{2\mu_i}{\alpha_i^2}\left(\bar{\lambda}_1^{\alpha_i} + \bar{\lambda}_2^{\alpha_i} + \bar{\lambda}_3^{\alpha_i} - 3\right) + \sum_{i=1}^{N} \frac{1}{D_i}\left(J^{el} - 1\right)^{2i} \tag{1}$$

where $\bar{\lambda}_i$ is the deviatoric principal stretches, $\bar{\lambda}_i = J^{-1/3}\lambda_i$ and λ_i is the principal stretches. The initial shear modulus and bulk modulus for the Ogden form are given by $\mu_0 = \sum_{i=1}^{N} \mu_i$ and $K_0 = 2/D_1$. Here N = 3, and the material parameters are listed in Table 1 [55]. Note that in order to determine its bulk modulus, we set its bulk modulus to 20 times its shear modulus and make this material have some compressibility.

As shown in Fig. 1, the geometrical parameters are listed as below: L = 100 mm, h = 5 mm, D = 65 mm, R = 12.5 mm and H = 20 mm. In this paper, the gas filled in the airbag is air. At standard atmospheric pressure (273.15 K and atmospheric pressure P_0 101.325 kPa), its density and molecular weight are 1.293 g/L and 28.9 g/mol, respectively. The absolute zero and gas constant are 0 K and 8.314 J/(mol K). In the simulation, the heat capacity at constant pressure must be specified when modeling an adiabatic process for the ideal gas. It can be defined in polynomial form based on the Shomate equation according to the National Institute of Standards and Technology and its parameters can refer to Supplementary Material S2 and [54].

The dynamic response of AMM can be tuned by tuning the gauge pressure or gas temperature in the airbag. The gauge pressure or change of gas temperature is applied to deform the unit cell of AMM, and then the propagation of elastic wave in the deformed unit cell of AMM is investigated. Thus, the computational analysis process can be divided into the following two steps: (1) structural deformation induced by gauge pressure or change of gas temperature and (2) wave propagation or vibration analysis. The commercial finite element code ABAQUS was used for simulating the inflation process of airbag and wave propagation analysis [54]. The finite element models of the frame structure and balancing weight are constructed by solid element C3D8 and C3D4, respectively. For the airbag, because of the ratio $t/R > 0.1$, its finite element model should be constructed by solid element C3D8R.

In the first step, because of the minor deformation of frame structure during inflation, to simplify the analysis, the symmetrical boundaries are adopted on the boundaries of frame structure. The inflation process of airbag is simulated with the help of the analysis technique of surface-based fluid modeling in ABAQUS. The *fluid cavity and *fluid inflator are adopted to model the fluid-filled structure and the actual inflator to inflate a fluid

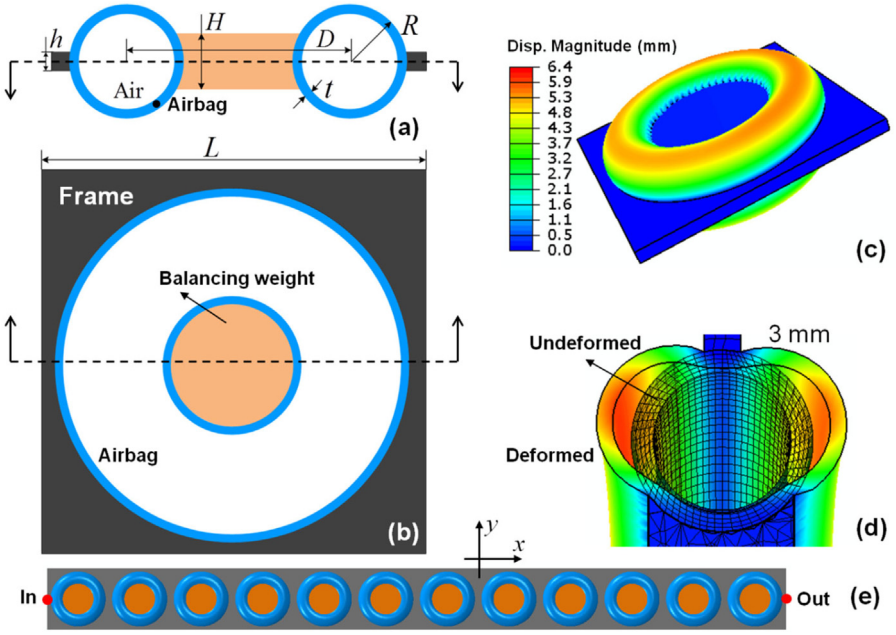

Fig. 1. The geometrical model of tunable acoustic metamaterial. (a) and (b) display the geometrical configuration. It consists of three parts: frame structure, airbag and balancing weight. Its dynamic response can be tuned through inflating air into the airbag. Meanwhile, given the mass of inflated air, adjusting gas temperature can also achieve the manipulation purpose of dynamic response. (c) is for the displacement field of AMM structure in the inflated state (thickness of airbag: 3 mm; mass of inflated air: 0.187 g; gauge pressure: 0.117 MPa; gas temperature: 25 °C) and (d) for the primitive and deformed cross-section configurations of airbag. (e) is for the finite-sized AMM structure consisting of 12 unit cells. In and Out denote the applied positions of load and the measure position of output, respectively.

cavity [54]. In the second step, the Bloch-type periodic boundary conditions are applied to the boundaries of frame structure to perform the frequency domain wave propagation or vibration analysis to obtain the dispersion relation. The detailed descriptions of inflation process and its implementation approach, wave propagation or vibration analysis and the corresponding numerical calculating procedure are provided in Supplementary Materials S2 and S3.

The thickness of airbag is t. In this paper, we design AMMs with $t = 3$ mm and $t = 4$ mm airbags, respectively. Keeping the outer diameter R of the airbag constant, their interior volumes V_0 are 5.79e4 and 4.64e4 mm^3, respectively. At standard atmospheric pressure, the mass of air m_0 in the airbag of stress-free state ($n = 0.0$, $T = 0$ °C) is 0.07486 g and 0.05993 g, respectively. After inflating air into the airbag, the total mass of air is assumed as m. Next, we will investigate the relationships of actual mass of inflated air ($m - m_0$), gauge pressure ($\triangle p$) in the airbag, gas temperature and cavity volume of airbag ($V = V_0 + \Delta V$, where V, V_0 and ΔV are the current volume, initial volume and change of volume of cavity). There is a variant balance among them. At a given gas temperature, the gauge pressure in the airbag can be determined by providing the mass of inflated air. Thus, in this paper, we study the effect of gauge pressure on the dynamic performance of AMM by giving the mass of inflated air. Further, we will investigate the effects of gauge pressure and gas temperature on the dynamic performance of AMM.

3. Numerical results and discussion

3.1. Relationships of airbag state parameters and structural stiffness

3.1.1. Relationships of airbag state parameters

In the process of inflation, the gauge pressure leads to the deformation of the airbag while the gauge pressure and the cavity volume also change until they reach a new balance. For example, Fig. 1(c) and (d) show the deformed configuration of AMM with a 3 mm airbag when the mass of inflated air, gauge pressure and gas temperature in the airbag are 0.187 g, 0.117 MPa, 25 °C, respectively. It can be seen that the cavity volume of airbag significantly increases after inflation. Later we will see that this deformation can significantly tune the dynamic response of AMM. Here, in order to quantificationally depict the change relationships of the state parameters of airbag such as mass of inflated air ($m-m_0$), gauge pressure ($\triangle p$), gas temperature and cavity volume of airbag (V) during inflation, the dimensionless indexes such as dimensionless gauge pressure $\Delta p/P_0$, dimensionless change of cavity volume $\Delta V/V_0$ and dimensionless mass of inflated air $n = m/m_0 - 1$ are adopted. The actual data of gauge pressure and cavity volume at specify temperature and mass of inflated air is listed in Tables S3 and S4 of Supplementary Materials. Fig. 2 shows the changes in the relationship among them. Fig. 2(a) and (b) are for the AMMs with 3 mm and 4 mm airbags, respectively. As shown in Fig. 2, at the given temperature and dimensionless mass of inflated air (n), the dimensionless gauge pressure $\Delta p/P_0$ and the dimensionless change of cavity volume $\Delta V/V_0$ can be determined. Because the thicker airbag can withstand more significant inflation pressure, the gauge pressure in a 4 mm airbag is more significant than that in a 3 mm airbag. It is obvious that both the dimensionless gauge pressure $\Delta p/P_0$ and the dimensionless change of cavity volume $\Delta V/V_0$ increase with increase of gas temperature and mass of inflated air (nm_0). In addition, it can be observed that the change of gauge pressure decreases with the increase of mass of inflated air. The gauge pressure and change of cavity volume curves in the same mass of inflated air are linear versus gas temperature. On the basis of Fig. 2, Fig. 3(a) shows the relationship curves of gauge pressure and change of cavity volume. In this figure, the same identifiers on the same line denote the starting and end points of this line. It can be seen that there is a significant nonlinear relationship between gauge pressure and change of cavity volume. This is mainly because of the nonlinear relationship between gauge pressure and mass of inflated air (refer to Supplementary Material S2).

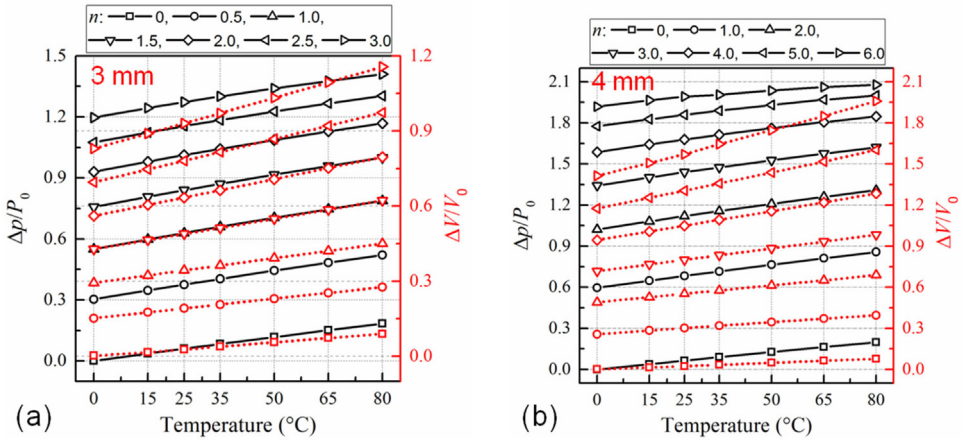

Fig. 2. The relationships of the dimensionless gauge pressure, dimensionless change of cavity volume, gas temperature and dimensionless mass of inflated air in the steady state. (a) is for AMM with a 3 mm airbag and (b) for AMM with a 4 mm airbag, respectively. The black and red lines correspond to the dimensionless gauge pressure and change of cavity volume, respectively. The actual data of gauge pressure and cavity volume at specify temperature and mass of inflated air is listed in Tables S3 and S4 in Supplementary Materials.

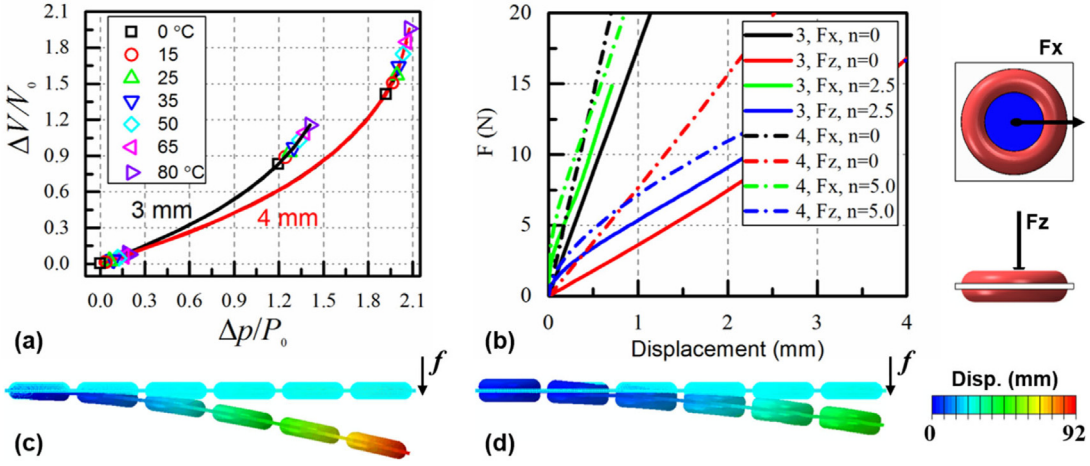

Fig. 3. (a) The relationships of dimensionless gauge pressure and dimensionless change of cavity volume at the given temperatures. The same identifiers on the same line denote the starting and end points of this line, respectively. The black and red lines correspond to AMM with 3 mm and 4 mm airbags, respectively. (b) is for the displacement–force relationships of airbag in the uninflated ($n = 0, T = 0$ °C) and inflated ($T = 25$ °C) configurations. (c) and (d) are for the bending deformations of the uninflated ($n = 0, T = 0$ °C) and inflated ($n = 2.5, T = 25$ °C) cantilever AMM structure consisting of 6 unit cells with a 3 mm airbag under the same load (0.05 MPa/mm^2), respectively.

3.1.2. Discussion of structural stiffness

Further, the gauge pressure in the airbag can lead to the change of structural stiffness of airbag, which can be used to manipulate the dynamic performance of AMM. Because of the nonlinear hyperelasticity of airbag material, it is difficult to describe quantitatively the change of structural stiffness of airbag during inflation. Here, we will qualitatively represent the structural stiffness of airbag in the uninflated ($n = 0, T = 0$ °C) and inflated ($T = 25$ °C) configurations. Following $f = k \cdot x$, the equivalent longitudinal and transverse stiffness are measured through given the applied concentrated force f. x is the measured small displacement. Fig. 3(b) shows the displacement–force relationships in the uninflated and inflated states, respectively. It can be observed that in the uninflated state, the structural stiffness of airbag is in linear elastic state. The structural stiffness in the x-direction is more significant than that in the z-direction. And the structural stiffness of the airbag of 4 mm is greater than that of 3 mm. However, in the inflated configuration, the material parameters of the airbag are changed because of its hyperelasticity, and thus its structural stiffness is also changed. It can be seen from Fig. 3(b) that in the inflated state the displacement–force relations exhibit significant nonlinearities. However, it can be qualitatively gotten that the structural stiffness in the x-direction is still greater than that in the z-direction. Meanwhile, the structural stiffness in the inflated state is greater than that in the uninflated state.

Also, the airbag can be regarded as a variable stiffness inclusion, and it is embedded into the frame structure. The airbag and frame structure couples together. During inflation, the change of structural stiffness of the airbag leads to a significant shift in out-of-plane structural stiffness of frame structure. As shown in Fig. 3(c) and (d), it can be seen that under the same load (0.05 MPa/mm^2), the deflection of finite-sized AMM structure in the inflated ($n = 2.5, T = 25$ °C) state is much less than that in the uninflated ($n = 0, T = 0$ °C) state, which indicates the bending stiffness of frame structure is significantly increased after inflation. However, the in-plane structural stiffness of frame structure is mainly determined by its own stiffness before and after inflation. Later, the result of mode analysis indicates that the in-plane torsional stiffness of the airbag decreases with increase of gauge pressure because the thickness of the airbag becomes thin after inflation. In the following, we will note that the changes

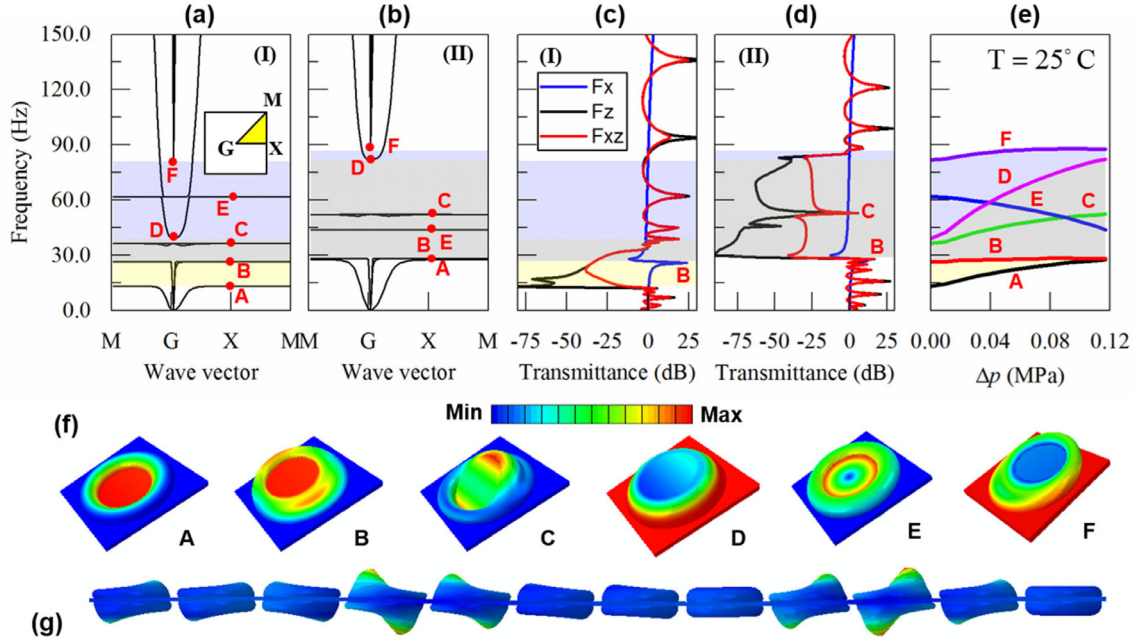

Fig. 4. (a) and (b) are for the band structures of AMMs with the airbag of thickness 3 mm in the uninflated (I, $n = 0, T = 25$ °C) and inflated (II, $n = 2.5, T = 25$ °C) states, respectively, and (c) and (d) show their transmittances in the finite-sized AMM structures consisting of 12 unit cells, respectively. The gauge pressures are 0.00609 MPa and 0.11704 MPa, respectively. (e) shows the evolution of mode frequencies and band gaps in the band structure versus gauge pressure in the airbag. A, B, C, D, E and F denote the mode frequencies of choice, and (f) shows their Bloch mode shapes at these frequency points of choice. A, B, C and E is at X, and D and F at G. The inset map in (a) shows the first Brillouin zone (square area) and irreducible Brillouin zone (Triangle GXM). (I) and (II) denote the uninflated and inflated configurations of an airbag, respectively. Because of the symmetry of unit cell, there are repeated frequency modes (at B, C and F) in the band structure. These mode frequencies at A, B, C, D, E and F are listed in Supplementary Material S4. Frequency range A∼D corresponds to the out-of-plane band gap and B∼F to in-plane band gap. (g) shows the mode shape of the finite-sized structure at mode frequency C (53 Hz). Fx, Fz and Fxz represent applied *x*-axis, *z*-axis and xz-direction loads.

of structural stiffness of airbag and frame structure during inflation determine the tunability of the dynamic performance of AMM.

3.2. Characteristics and manipulation of band structure

3.2.1. Characteristics of band structure of AMMs

Next, we will investigate the effects of gauge pressure on the band structures of AMMs and the transmittances of finite-sized AMM structures. Figs. 4 and 5 show the calculation results of AMMs with 3 mm and 4 mm airbags, respectively. Fig. 4(a) and (b) show the band structures of AMM in the uninflated ($n = 0, T = 25$ °C) and inflated ($n = 2.5, T = 25$ °C) configurations, respectively. Correspondingly, Fig. 4(c) and (d) show their transmittances of finite-sized AMM structures. Further, Fig. 4(e) displays the evolution of band gaps versus gauge pressure. Fig. 4(a)∼(e) have the same *y*-axis and symbols A, B, C, D, E and F in them denote the mode frequency points of choice. A, B, C and E locate at X, and D and F locate at G. Fig. 5 follows the same description. Fig. 4(f) exhibits the mode shapes at these frequency points. The flat modes A, B, C and E correspond to the locally resonant mode of balancing weight, and modes D and F correspond to the Lamb mode of frame structure [5]. For AMM with a 4 mm airbag, it has the same mode shapes at the same tagged frequencies in Fig. 5 and thus they are not repeated. Because of the symmetry of unit cell, there are repeated mode frequencies. The repeated mode frequencies locate at mode B, C and F in Figs. 4 and 5. For example, point B, point C and point F in Fig. 4(a) have the repeated frequencies: 26.68 Hz, 36.49 Hz and 81.83 Hz, respectively, and in Fig. 4(b) have the repeated frequencies: 28.45 Hz, 52.31 Hz and 87.59 Hz, respectively.

The band gaps in Figs. 4 and 5 include the in-plane band gap (B∼F) and out-of-plane band gap (A∼D). Their overlapping range is the complete band gap (B∼D). Taking AMM with a 3 mm airbag as an example, as shown in Fig. 4(a), the out-of-plane band gap is at 13.37 Hz∼39.17 Hz (A∼D) and the in-plane band gap is at 26.68 Hz∼81.83 Hz (B∼F). Their relative band widths (defined as the ratio between the band gap width and the center frequency of the band) are about 0.982 and 1.016, respectively. After inflation, these band gaps shift to 27.59 Hz∼82.16 Hz (A∼D) and 28.45 Hz∼87.59 Hz (B∼F), respectively, as shown in Fig. 4(b). Their relative band widths are about 0.994 and 1.019, respectively. The overlapping frequency ranges (B∼D) of out-of- and in-plane band gaps are 26.68 Hz∼39.17 Hz and 28.45 Hz∼82.16 Hz before and after inflation, which are their complete band gap. For AMM with a 4 mm airbag, it has the same characteristic. The detailed mode frequencies at A, B, C, D, E and F are listed in Supplementary Material S4.

For the finite-sized AMM structure, it can be seen from Fig. 4(c) and (d) that only applying out-of-plane load (along *z*-axis, Fz), its transmittances are significantly reduced in the out-of-plane band gap frequency range (A∼D). Meanwhile, under in-plane load (along *x*-axis, Fx), its in-plane transmittances in the in-plane band gap frequency range (B∼F) are less than those in other frequency ranges. Under both out-of- and in-plane load (Fxz), its transmittances are still reduced significantly in the band gap frequency range, but the effectiveness of suppression is less than that only under out-of-plane load because of the influence of in-plane load. In short, the transmittances of finite-sized AMM structures are significantly reduced in the band gap frequency range, which agrees well with the prediction of band structure in Fig. 4(a) and (b). In addition, in these frequency ranges, the passing frequency points such as C and E are almost single frequency points and thus they have almost no influence on the band gaps. However, their influences can be observed from the transmittances of finite-sized AMM structures. Later, we will explain the roles of these frequency points in the formation of band gaps. From Fig. 5(c) and (d), the same phenomena can be observed.

We can assure now that the tunable gauge pressure can be used to tune the dynamic responses of AMM. To reveal the manipulation performance of band gap through tunable gauge pressure, Figs. 4(e) and 5(e) exhibit the evolutions of mode frequencies and band gaps versus gauge pressure in the airbag. It can be seen that modes A, C and D shift to high frequency, and modes B and F almost keep constant. Differently, for mode E, its mode frequency shifts to low-frequency with the increase of gauge pressure. Thus, the out-of-plane band gap (A∼D) moves to high-frequency with the increase of gauge pressure while its width increases, but the in-plane band gap (B∼F) almost keeps constant. Just because of these, the complete band gap (B∼D) shifts to the high-frequency range with the increase of gauge pressure. Based on these calculation results above, next we will further analyze the formation and manipulation mechanism of band gaps and investigate the roles of each mode in the formation of band gaps.

3.2.2. Formation and manipulation mechanism of band gaps

3.2.2.1. Mode A and mode D. Next, we will reveal the role of each of the modes (A, B, C, D, E, and F) in the formation of the band gap. As shown in Fig. 4(f), for the flat mode A, the balancing weight vibrates along the z-axis (out-of-plane) while the frame structure remains stationary. At this frequency, the vibrating balancing weight applies a reacting force to the frame structure so that the out-of-plane waves cannot propagate through the AMM structure. At this mode frequency point, the out-of-plane band gap (A∼D) is opened. On the contrary, the mode D corresponds to an anti-symmetric Lamb mode of the frame structure. The balancing weight remains stationary at this frequency, but the out-of-plane anti-symmetric Lamb mode of the frame structure is activated so that the out-of-plane waves can propagate through the AMM structure. At this mode frequency point, the out-of-plane band gap (A∼D) is closed. The formation of the out-of-plane band gap (A∼D) is due to the coupling between the out-of-plane flat mode (A) of balancing weight and anti-symmetric Lamb mode (D) of the frame structure.

It can be seen from Figs. 4(e) and 5(e) that the mode frequencies A and D move to high-frequency with the increase of gauge pressure. And the increase of mode frequency D is greater than that of mode frequency A so that this out-of-plane band gap (A∼D) shifts to high frequency and its width increases drastically during inflation. As mentioned above, the tunable gauge pressure can change the structural stiffness of the airbag and frame stiffness. Mode A relates to the out-of-plane structural stiffness of the airbag, and mode D relates to the structural bending stiffness of frame structure. During inflation, their structural stiffness increases so that the mode frequencies A and D relating them shift to high-frequency. Just because of these effects, the out-of-plane band gap is significantly manipulated during inflation.

3.2.2.2. Mode B and mode F. As shown in Fig. 4(f), the flat mode B corresponds to in-plane vibration mode of balancing weight. Similarly, at this frequency the in-plane vibrating balancing weight applies a reacting force to the frame structure so that the in-plane waves cannot propagate through the AMM structure. At this mode frequency, the in-plane band gap (B∼F) is opened. Correspondingly, mode F corresponds to the in-plane symmetric Lamb mode of frame structure. At mode F, the balancing weight remains stationary while the frame structure vibrates in-plane. Because the resonant mode F is activated, the in-plane wave can propagate through the AMM structure so that the in-plane band gap (B∼F) is closed. Then, the existent of in-plane band gap (B∼F) is due to the coupling between the in-plane resonant mode of balancing weight and the in-plane symmetric Lamb mode of frame structure.

It can be seen from Figs. 4(e) and 5(e) that the mode frequencies B and F have tiny changes during inflation. They are closely related to the in-plane structural stiffness of airbag and frame structure. As mentioned above, the in-plane structural stiffness of airbag and frame structure has tiny changes during inflation, so that the mode frequencies related to them only have small differences. Thus, the in-plane band gap (B∼F) almost keeps constant during inflation. However, the complete band gap (B∼D) is the overlapping frequency range, and therefore the increase of this band gap (B∼D) is mainly due to the rise of the out-of-plane band gap during inflation.

3.2.2.3. Mode E. Mode E corresponds to the in-plane rotation of balancing weight, as shown in Fig. 4(f). This vibration of balancing weight is non-coupling with the frame structure, and this means that no reacting force is applied to the frame structures, so that this type of vibration mode has no contribution to the formation of band gaps. As shown in Figs. 4(e) and 5(e), this mode frequency moves to low-frequency with the increase of gauge pressure. This is mainly because, during inflation, the thickness of the airbag becomes thin so that the torsional stiffness of the airbag decreases (refer to Supplementary Material S8).

3.2.2.4. Mode C. Mode C corresponds to the rotation of balancing weight around a specific axis paralleling to the x–y plane, as shown in Fig. 4(f). The areas of positive and negative vibrations and their amplitudes are the same so that no z-direction reacting force is applied to the frame structures. Thus, this vibration mode still has no contribution to the formation of out-of-plane band gaps. However, its effect on the transmittance of finite-sized AMM structure can be observed from Figs. 4(d) and 5(d). As shown in Figs. 4(d) and 5(d), there is a peak of transmittance at frequency C. Namely, and the out-of-plane waves can propagate through the AMM structure at this frequency. Fig. 4(g) shows the vibration mode of the finite-sized AMM structure at this frequency (53 Hz). The balancing weights vibrate as the same as the prediction shown in Fig. 4(f). Because of the rotation vibration of balancing weight, the waves are propagated downstream. Similar to mode A, this mode relates to the structural stiffness of the airbag. The increase of out-of-plane structural stiffness after inflation leads to the rise of this mode frequency.

In short, the formations of out-of-plane and in-plane band gaps are closely related to the structural stiffness of airbag and frame structure. They determine the flat mode (A and B) of balancing weight and Lamb mode (D and F) of frame structure [5], respectively. During inflation, their structural stiffness is changed so that the out-of-plane and in-plane band gaps can be tuned. The complete band gap is the overlapping frequency range and its manipulation is mainly determined by the anti-symmetric Lamb mode (D) of frame structure.

3.3. Effect of gas temperature on band structures of AMM

Fig. 2 have shown the relationships of the dimensionless gauge pressure, dimensionless change of cavity volume, gas temperature, and mass of inflated air in the steady-state. It can be seen that the gauge pressure in the airbag increases with the increase in gas temperature. Thus, similar to the above gauge pressure control strategy, we can consider utilizing temperature to manipulate the dynamic performance of AMM.

Here, to study the effect of gas temperature on the dynamic performance of AMM, the mass of inflated air is given. For the AMM with a 3 mm airbag, the given dimensionless mass of inflated air is $n = 0.5$ and $n = 2.0$, respectively, and for that with a 4 mm airbag, the given dimensionless mass of inflated air is $n = 1.0$ and $n = 5.0$, respectively. Fig. 6(a) and (b) and Fig. 6(c) and (d) show the band structures of AMM with 3 mm and 4 mm airbag in

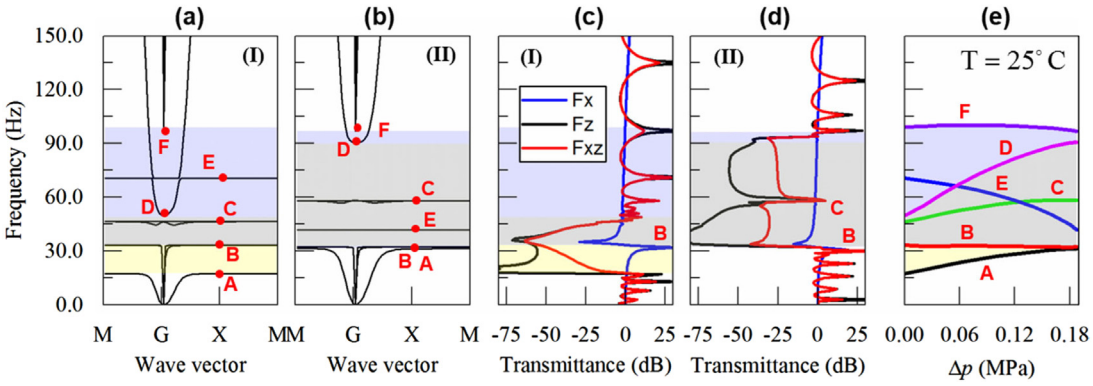

Fig. 5. (a) and (b) are for the band structures of AMMs with the airbag of thickness 4 mm in the uninflated (I, $n = 0, T = 25$ °C) and inflated (II, $n = 5.0, T = 25$ °C) states, respectively, and (c) and (d) show their transmittances in the finite-sized AMM structures, respectively. The gauge pressures are 0.00653 MPa and 0.18835 MPa, respectively. (e) shows the evolution of mode frequencies and band gaps in the band structure versus gauge pressure in the airbag. Implications of symbols in this figure are the same as those in Fig. 4. The mode shape of each mode is the same as Fig. 4(f). The mode frequencies at these symbols are listed in Supplementary Material S4.

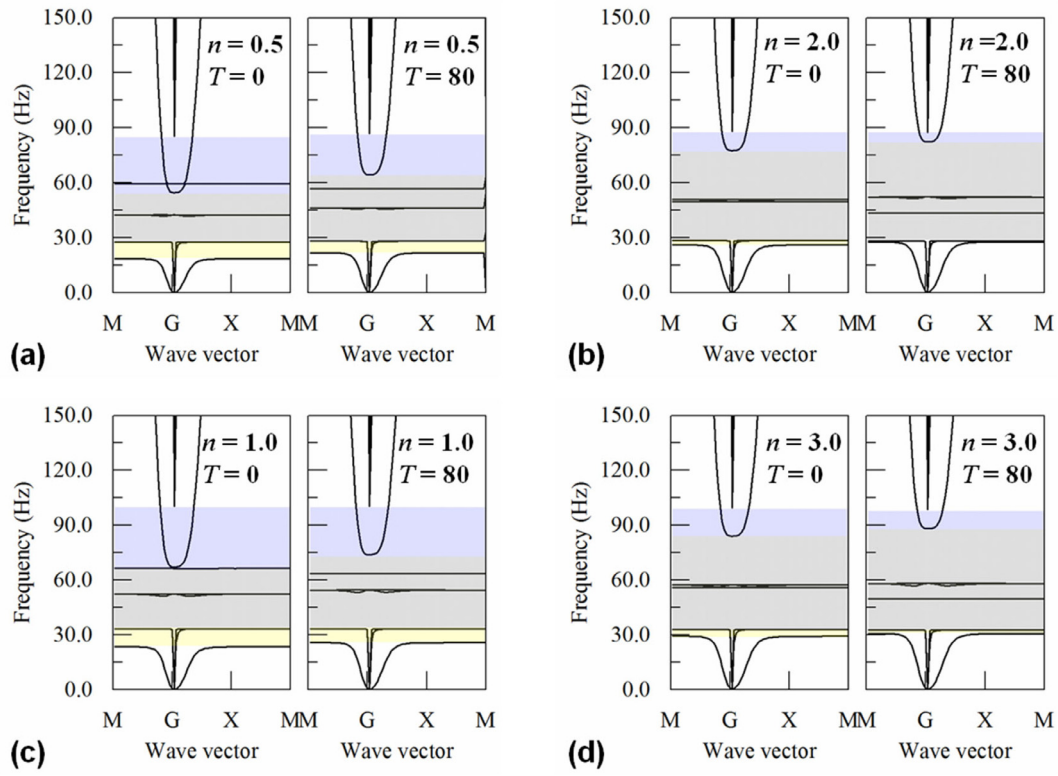

Fig. 6. Effects of temperature on the low-frequency band structures of AMMs. (a) and (b) are for AMM with a 3 mm airbag, (c) and (d) for that with a 4 mm airbag. (a) $n = 0.5, T = 0$ °C,$T = 80$ °C; (b) $n = 2.0, T = 0$ °C,$T = 80$ °C; (c) $n = 1.0, T = 0$ °C,$T = 80$ °C; (d) $n = 5.0, T = 0$ °C,$T = 80$ °C.

0 °C and 80 °C gas temperatures, respectively. It can be seen from Fig. 6 that the in-plane band gaps are almost unrelated to the gas temperature. However, the temperature can significantly alter the positions and widths of the out-of-plane band gaps. For example, in Fig. 6(a), the out-of-plane band gaps are at 18.5 Hz∼54.5 Hz and 21.8 Hz∼64.5 Hz at 0 °C and 80 °C, respectively. And the corresponding complete band gaps are at 28.2 Hz∼54.5 Hz and 28.2 Hz∼64.5 Hz, respectively. In Fig. 6(b), the out-of-plane band gaps are at 26.0 Hz∼77.5 Hz and 27.5 Hz∼82.4 Hz at 0 °C and 80 °C, respectively. And the corresponding complete band gaps are at 28.5 Hz∼77.5 Hz and 28.4 Hz∼82.4 Hz, respectively. The temperature can effectively tune the dynamic performance of AMM. With the increase of gas temperature, the band gaps shift to high-frequency, and their widths increase. Also, we find that the higher the inflation pressure in the airbag is, the lower the manipulation of the dynamic performance of AMM through temperature is. These same conclusions can be further verified from Fig. 6(c) and (d). The formation and manipulation mechanism of band gap through temperature manipulation is the same as through tunable gauge pressure manipulation.

At last, it is worth noting that besides the effect of gauge pressure and gas temperature on the low-frequency band gaps above, the high-frequency band structures can also be tuned (refer to Supplementary Material S5 and S6). The high-frequency modes mainly reflect the dynamic characteristics of airbag structures, and these modes of vibration are dense and complex. For the designed AMM structure and the used material model, with increases of inflation pressure and gas temperature, the high-frequency mode frequencies shift to low-frequency because of the

decrease of structural stiffness and the increase of the geometrical size of the airbag after inflation.

In short, the dynamic performance of the AMMs presented in this paper can be manipulated through tuning gauge pressure and gas temperature. Especially, their low-frequency band gaps can be effectively manipulated to be used for the active control of low-frequency vibration and noise.

4. Conclusions and discussion

In this paper, a kind of AMMs consisting of the frame structure, airbag, and balancing weight are designed to suppress the low-frequency vibration and noise. The band structures of AMM in different gauge pressures and gas temperatures are calculated, and numerical calculations analyze the formation and manipulation mechanism of band gaps. The following conclusions can be gotten:

1. The formation of an out-of-plane band gap is due to the coupling between the out-of-plane resonant mode of balancing weight and the anti-symmetric Lamb mode of the frame structure. And the formation of the in-plane band gap is due to the coupling between the in-plane resonant mode of balancing weight and the symmetric Lamb mode of the frame structure. The overlapping frequency range of out-of- and in-plane band gaps is the complete band gap.
2. The manipulation mechanism of band gaps stems from the changes of structural stiffness of airbag and frame structure through tunable gauge pressure and change of temperature. The resonant modes of balancing weight relate to the in-plane, out-of-plane and torsional stiffness of the airbag. The Lamb modes of balancing weight relate to the in-plane and bending stiffness of frame structure. The gauge pressure and change of air temperature can change the structural stiffness associated with the above structural modes so that their structural modes can be tuned.
3. The AMM can manipulate ultralow-frequency band gaps about 13 Hz∼90 Hz, and they can be used for low-frequency vibration and noise control. The gauge pressure and gas temperature mainly tune the out-of-plane band gaps.

The resonant element consisting of airbag and balancing weight can be used to design other forms of AMMs. For example, the resonant element can be embedded into a sandwich structure to form the sandwich AMM possessing a low-frequency band gap. Also, the airbag and the holes (used to fix the airbag) in the frame structure can be designed in other forms so that the AMM has other dynamic performance, such as anisotropy. In the follow-up study, the gas viscosity and material viscosity should be considered, which may affect the dynamic performance of AMM.

Declaration of competing interest

The authors declare that they have no known competing financial interests or personal relationships that could have appeared to influence the work reported in this paper.

Acknowledgments

This work is supported by the Science Challenge Project, China, No. TZ2018002, National Natural Science Foundation of China, under Grant No. 11972205 and 11722218, the National Key Research Development Program of China (No. 2017YFB0702003), Opening Project of Applied Mechanics and Structure Safety Key Laboratory of Sichuan Province.

Appendix A. Supplementary data

Supplementary material related to this article can be found online at https://doi.org/10.1016/j.eml.2021.101218.

References

[1] V.M. García-Chocano, J. Christensen, J. Sánchez-Dehesa, Negative refraction and energy funneling by hyperbolic materials: An experimental demonstration in acoustics, Phys. Rev. Lett. 112 (2014) 144301, http://dx.doi.org/10.1103/PhysRevLett.112.144301.

[2] R. Zhu, X.N. Liu, G.K. Hu, C.T. Sun, G.L. Huang, Negative refraction of elastic waves at the deep-subwavelength scale in a single-phase metamaterial, Nature Commun. 5 (2014) 5510, http://dx.doi.org/10.1038/ncomms6510.

[3] M.-H. Lu, C. Zhang, L. Feng, J. Zhao, Y.-F. Chen, Y.-W. Mao, J. Zi, Y.-Y. Zhu, S.-N. Zhu, N.-B. Ming, Negative birefraction of acoustic waves in a sonic crystal, Nature Mater. 6 (2007) 744–748, http://dx.doi.org/10.1038/nmat1987.

[4] I. Pérez-Arjona, V.J. Sánchez-Morcillo, J. Redondo, V. Espinosa, K. Staliunas, Theoretical prediction of the nondiffractive propagation of sonic waves through periodic acoustic media, Phys. Rev. B 75 (2007) 014304, http://dx.doi.org/10.1103/PhysRevB.75.014304.

[5] S. Li, T. Chen, X. Wang, Y. Li, W. Chen, Expansion of lower-frequency locally resonant band gaps using a double-sided stubbed composite phononic crystals plate with composite stubs, Phys. Lett. A 380 (2016) 2167–2172, http://dx.doi.org/10.1016/j.physleta.2016.03.027.

[6] Z. Liu, Locally resonant sonic materials, Science (80-.) 289 (2000) 1734–1736, http://dx.doi.org/10.1126/science.289.5485.1734.

[7] Y. Ding, Z. Liu, C. Qiu, J. Shi, Metamaterial with simultaneously negative bulk modulus and mass density, Phys. Rev. Lett. 99 (2007) 093904, http://dx.doi.org/10.1103/PhysRevLett.99.093904.

[8] S.H. Lee, C.M. Park, Y.M. Seo, Z.G. Wang, C.K. Kim, Composite acoustic medium with simultaneously negative density and modulus, Phys. Rev. Lett. 104 (2010) 054301, http://dx.doi.org/10.1103/PhysRevLett.104.054301.

[9] M. Yang, G. Ma, Z. Yang, P. Sheng, Coupled membranes with doubly negative mass density and bulk modulus, Phys. Rev. Lett. 110 (2013) 134301, http://dx.doi.org/10.1103/PhysRevLett.110.134301.

[10] N. Fang, D. Xi, J. Xu, M. Ambati, W. Srituravanich, C. Sun, X. Zhang, Ultrasonic metamaterials with negative modulus, Nature Mater. 5 (2006) 452–456, http://dx.doi.org/10.1038/nmat1644.

[11] Y. Chen, G. Hu, G. Huang, A hybrid elastic metamaterial with negative mass density and tunable bending stiffness, J. Mech. Phys. Solids 105 (2017) 179–198, http://dx.doi.org/10.1016/j.jmps.2017.05.009.

[12] M. Dubois, C. Shi, X. Zhu, Y. Wang, X. Zhang, Observation of acoustic Dirac-like cone and double zero refractive index, Nature Commun. 8 (2017) 14871, http://dx.doi.org/10.1038/ncomms14871.

[13] Z. He, K. Deng, H. Zhao, X. Li, Designable hybrid sonic crystals for transportation and division of acoustic images, Appl. Phys. Lett. 101 (2012) 243510, http://dx.doi.org/10.1063/1.4772205.

[14] F. Casadei, T. Delpero, A. Bergamini, P. Ermanni, M. Ruzzene, Piezoelectric resonator arrays for tunable acoustic waveguides and metamaterials, J. Appl. Phys. 112 (2012) 064902, http://dx.doi.org/10.1063/1.4752468.

[15] J. Zhu, J. Christensen, J. Jung, L. Martin-Moreno, X. Yin, L. Fok, X. Zhang, F.J. Garcia-Vidal, A holey-structured metamaterial for acoustic deep-subwavelength imaging, Nat. Phys. 7 (2011) 52–55, http://dx.doi.org/10.1038/nphys1804.

[16] M. Molerón, C. Daraio, Acoustic metamaterial for subwavelength edge detection, Nature Commun. 6 (2015) 8037, http://dx.doi.org/10.1038/ncomms9037.

[17] S. Zhang, C. Xia, N. Fang, Broadband acoustic cloak for ultrasound waves, Phys. Rev. Lett. 106 (2011) 024301, http://dx.doi.org/10.1103/PhysRevLett.106.024301.

[18] Y. Bi, H. Jia, W. Lu, P. Ji, J. Yang, Design and demonstration of an underwater acoustic carpet cloak, Sci. Rep. 7 (2017) 705, http://dx.doi.org/10.1038/s41598-017-00779-4.

[19] Y. Xie, W. Wang, H. Chen, A. Konneker, B.-I. Popa, S.A. Cummer, Wavefront modulation and subwavelength diffractive acoustics with an acoustic metasurface, Nature Commun. 5 (2014) 5553, http://dx.doi.org/10.1038/ncomms6553.

[20] H. Zhang, J. Wen, Y. Xiao, G. Wang, X. Wen, Sound transmission loss of metamaterial thin plates with periodic subwavelength arrays of shunted piezoelectric patches, J. Sound Vib. 343 (2015) 104–120, http://dx.doi.org/10.1016/j.jsv.2015.01.019.

[21] F. Javid, P. Wang, A. Shanian, K. Bertoldi, Architected materials with ultralow porosity for vibration control, Adv. Mater. 28 (2016) 5943–5948, http://dx.doi.org/10.1002/adma.201600052.

[22] M.I. Hussein, M.J. Leamy, M. Ruzzene, Dynamics of phononic materials and structures: Historical origins, recent progress, and future outlook, Appl. Mech. Rev. 66 (2014) 040802, http://dx.doi.org/10.1115/1.4026911, (38 pages).
[23] Z. Liu, C.T. Chan, P. Sheng, Analytic model of phononic crystals with local resonances, Phys. Rev. B 71 (2005) 014103, http://dx.doi.org/10.1103/PhysRevB.71.014103.
[24] B. Xia, N. Chen, L. Xie, Y. Qin, D. Yu, Temperature-controlled tunable acoustic metamaterial with active band gap and negative bulk modulus, Appl. Acoust. 112 (2016) 1–9, http://dx.doi.org/10.1016/j.apacoust.2016.05.005.
[25] Y. Xiao, J. Wen, X. Wen, Sound transmission loss of metamaterial-based thin plates with multiple subwavelength arrays of attached resonators, J. Sound Vib. 331 (2012) 5408–5423, http://dx.doi.org/10.1016/j.jsv.2012.07.016.
[26] S. Brûlé, E.H. Javelaud, S. Enoch, S. Guenneau, Experiments on seismic metamaterials: Molding surface waves, Phys. Rev. Lett. 112 (2014) 133901, http://dx.doi.org/10.1103/PhysRevLett.112.133901.
[27] Y. Achaoui, B. Ungureanu, S. Enoch, S. Brûlé, S. Guenneau, Seismic waves damping with arrays of inertial resonators, Extrem. Mech. Lett. 8 (2016) 30–37, http://dx.doi.org/10.1016/j.eml.2016.02.004.
[28] Y. Liu, J. Huang, Y. Li, Z. Shi, Trees as large-scale natural metamaterials for low-frequency vibration reduction, Constr. Build. Mater. 199 (2019) 737–745, http://dx.doi.org/10.1016/j.conbuildmat.2018.12.062.
[29] Y. Huang, C.L. Zhang, W.Q. Chen, Tuning band structures of two-dimensional phononic crystals with biasing fields, J. Appl. Mech. 81 (2014) http://dx.doi.org/10.1115/1.4027915.
[30] P.I. Galich, S. Rudykh, Manipulating pressure and shear waves in dielectric elastomers via external electric stimuli, Int. J. Solids Struct. 91 (2016) 18–25, http://dx.doi.org/10.1016/j.ijsolstr.2016.04.032.
[31] M. Schaeffer, M. Ruzzene, Wave propagation in multistable magneto-elastic lattices, Int. J. Solids Struct. 56–57 (2015) 78–95, http://dx.doi.org/10.1016/j.ijsolstr.2014.12.003.
[32] K. Yu, N.X. Fang, G. Huang, Q. Wang, Magnetoactive acoustic metamaterials, Adv. Mater. 30 (2018) 1706348, http://dx.doi.org/10.1002/adma.201706348.
[33] Q. Zhang, Y. Chen, K. Zhang, G. Hu, Programmable elastic valley hall insulator with tunable interface propagation routes, Extrem. Mech. Lett. 28 (2019) 76–80, http://dx.doi.org/10.1016/j.eml.2019.03.002.
[34] J. Xu, J. Tang, Tunable prism based on piezoelectric metamaterial for acoustic beam steering, Appl. Phys. Lett. 110 (2017) 181902, http://dx.doi.org/10.1063/1.4982717.
[35] E.G. Barnwell, W.J. Parnell, I.D. Abrahams, Tunable elastodynamic band gaps, Extrem. Mech. Lett. 12 (2017) 23–29, http://dx.doi.org/10.1016/j.eml.2016.10.009.
[36] P.I. Galich, N.X. Fang, M.C. Boyce, S. Rudykh, Elastic wave propagation in finitely deformed layered materials, J. Mech. Phys. Solids 98 (2017) 390–410, http://dx.doi.org/10.1016/j.jmps.2016.10.002.
[37] Y. Liu, Z. Chang, X.-Q. Feng, Stable elastic wave band-gaps of phononic crystals with hyperelastic transformation materials, Extrem. Mech. Lett. 11 (2017) 37–41, http://dx.doi.org/10.1016/j.eml.2016.11.007.
[38] H. Dong, F. Wu, H. Zhong, X. Zhang, Y. Yao, Effects of asymmetrical rotated rectangular basis on the acoustic band gap in two-dimensional acoustic crystals: the bands are twisted, J. Phys. D. Appl. Phys. 43 (2010) 105404, http://dx.doi.org/10.1088/0022-3727/43/10/105404.
[39] C. Goffaux, J.P. Vigneron, Theoretical study of a tunable phononic band gap system, Phys. Rev. B 64 (2001) 075118, http://dx.doi.org/10.1103/PhysRevB.64.075118.
[40] F. Wu, Z. Liu, Y. Liu, Acoustic band gaps created by rotating square rods in a two-dimensional lattice, Phys. Rev. E 66 (2002) 046628, http://dx.doi.org/10.1103/PhysRevE.66.046628.
[41] G.-Y. Li, G. Xu, Y. Zheng, Y. Cao, Non-leaky modes and bandgaps of surface acoustic waves in wrinkled stiff-film/compliant-substrate bilayers, J. Mech. Phys. Solids 112 (2018) 239–252, http://dx.doi.org/10.1016/j.jmps.2017.11.024.
[42] J. Li, Y. Wang, W. Chen, Y.-S. Wang, R. Bao, Harnessing inclusions to tune post-buckling deformation and bandgaps of soft porous periodic structures, J. Sound Vib. 459 (2019) 114848, http://dx.doi.org/10.1016/j.jsv.2019.114848.
[43] S. Ning, C. Luo, F. Yang, Z. Liu, Z. Zhuang, Mechanically tunable solid/solid phononic crystals through the rearrangement of hard scatterers controlled by the deformation of periodic elastomeric matrixes, J. Appl. Mech. 87 (2020) http://dx.doi.org/10.1115/1.4047365.
[44] S. Ning, F. Yang, C. Luo, Z. Liu, Z. Zhuang, Low-frequency tunable locally resonant band gaps in acoustic metamaterials through large deformation, Extrem. Mech. Lett. 35 (2020) 100623, http://dx.doi.org/10.1016/j.eml.2019.100623.
[45] S. Shan, S.H. Kang, P. Wang, C. Qu, S. Shian, E.R. Chen, K. Bertoldi, Harnessing multiple folding mechanisms in soft periodic structures for tunable control of elastic waves, Adv. Funct. Mater. 24 (2014) 4935–4942, http://dx.doi.org/10.1002/adfm.201400665.
[46] J. Shim, P. Wang, K. Bertoldi, Harnessing instability-induced pattern transformation to design tunable phononic crystals, Int. J. Solids Struct. 58 (2015) 52–61, http://dx.doi.org/10.1016/j.ijsolstr.2014.12.018.
[47] P. Wang, F. Casadei, S. Shan, J.C. Weaver, K. Bertoldi, Harnessing buckling to design tunable locally resonant acoustic metamaterials, Phys. Rev. Lett. 113 (2014) 014301, http://dx.doi.org/10.1103/PhysRevLett.113.014301.
[48] Y. Zheng, G.-Y. Li, Y. Cao, X.-Q. Feng, Wrinkling of a stiff film resting on a fiber-filled soft substrate and its potential application as tunable metamaterials, Extrem. Mech. Lett. 11 (2017) 121–127, http://dx.doi.org/10.1016/j.eml.2016.12.002.
[49] J. Meaud, Multistable two-dimensional spring-mass lattices with tunable band gaps and wave directionality, J. Sound Vib. 434 (2018) 44–62, http://dx.doi.org/10.1016/j.jsv.2018.07.032.
[50] C. Valencia, D. Restrepo, N.D. Mankame, P.D. Zavattieri, J. Gomez, Computational characterization of the wave propagation behavior of multi-stable periodic cellular materials, Extrem. Mech. Lett. 33 (2019) 100565, http://dx.doi.org/10.1016/j.eml.2019.100565.
[51] J. Meaud, K. Che, Tuning elastic wave propagation in multistable architected materials, Int. J. Solids Struct. 122–123 (2017) 69–80, http://dx.doi.org/10.1016/j.ijsolstr.2017.05.042.
[52] Z. Wu, Y. Zheng, K.W. Wang, Metastable modular metastructures for on-demand reconfiguration of band structures and nonreciprocal wave propagation, Phys. Rev. E 97 (2018) 022209, http://dx.doi.org/10.1103/PhysRevE.97.022209.
[53] Y. Huang, J. Li, W. Chen, R. Bao, Tunable bandgaps in soft phononic plates with spring-mass-like resonators, Int. J. Mech. Sci. 151 (2019) 300–313, http://dx.doi.org/10.1016/j.ijmecsci.2018.11.029.
[54] D.S. Abaqus, A. Fallis, D. Techniques, Abaqus analysis user's guide (6.14). Abaqus 6.12, 2013, http://dx.doi.org/10.1017/CBO9781107415324.004.
[55] G. Holzapfel, Nonlinear Solid Mechanics: A Continuum Approach for Engineering Science, Meccanica, 2002, http://dx.doi.org/10.1023/A:1020843529530.